Bunsen flame simulation by finite elements on adaptively refined, unstructured triangulations

Erik Burman†, Alexandre Ern‡‖ and Vincent Giovangigli§

† DMA, Ecole polytechnique fédérale de Lausanne, CH-1015, Switzerland
‡ CERMICS, Ecole nationale des ponts et chaussées, 6 et 8 avenue Blaise Pascal, F-77455 Marne la Vallée cedex 2, France
§ CMAP, Ecole polytechnique, F-91128 Palaiseau cedex, France

E-mail: erik.burman@epfl.ch, ern@cermics.enpc.fr, giovangi@cmapx.polytechnique.fr

Submitted to: *Combust. Theory Modelling*

Abstract. We investigate laminar bunsen flames with detailed chemistry and multicomponent transport. The governing equations are discretised by a finite element method on a sequence of adaptively refined, unstructured triangulations. The finite element method is an extension to chemically reacting flows of the streamline diffusion method, including least squares stabilisation of the pressure gradient and the low-Mach continuity equation as well as a shock capturing term designed to control species mass fraction undershoots near flame fronts. Unstructured meshes are adaptively refined based on a posteriori estimates of a user specified functional of the numerical error. These estimates are derived from the dual weighted residual method in the form of elementwise residuals weighted by coefficients depending on the solution of a linearised dual problem that accounts for convective error propagation and multicomponent chemistry couplings. Numerical results are presented to illustrate the efficiency of the proposed methodology and to study the impact of inflow velocity profiles on the structure of several hydrogen-air bunsen flames.

‖ Corresponding author

1. Introduction

Bunsen flames are obtained experimentally by flowing a premixed fuel/oxidiser jet through a cylindrical tube. When the jet velocity exceeds the laminar flame speed, it is possible under appropriate experimental conditions to stabilise a flame of conical shape above the tube lips. Bunsen flames arise in several practical applications including household and industrial burners. Furthermore, bunsen flames provide a relatively simple flow configuration on which to investigate fundamental aspects of laminar premixed combustion, including flame stabilisation mechanisms as well as chemically and hydrodynamically controlled extinction limits. The investigation of bunsen flame structures may also yield useful information to derive new, and improve current, premixed turbulent combustion models.

Despite the extensive progress witnessed over the last few years in computer technology, bunsen flame simulation still remains an extremely challenging task, especially when detailed chemistry modelling is taken into account. Computational difficulties stem from the disparity of time and space scales to be resolved and from the nonlinear couplings present in the governing equations. It is therefore critical to design reliable and efficient numerical methods that may achieve a prescribed level of accuracy at the lowest computational costs. A first important step in this direction is to optimise discrete degrees of freedom by using locally refined meshes. When the governing equations are discretised by finite difference methods, hierarchical meshes must be employed. Although hierarchical meshes offer some advantages, such as the possibility to construct smoothing operators within multigrid methods, fully unstructured meshes are particularly attractive because of their simplicity due to the absence of hanging nodes and their flexibility in handling complex geometries. Numerical methods well suited to fully unstructured meshes are finite element and finite volume methods.

In order to further reduce flame simulation costs, a highly desirable feature of a numerical method is its ability to provide a quantitative assessment of the computational error in the form of local error indicators. Such indicators provide information on the nature of the discrete solution and may therefore be used to construct adaptively refined meshes. A first strategy to design error indicators consists in using local estimates of the gradient and curvature of the numerical solution. Application to combustion problems includes [1, 2, 3, 4, 5, 6, 7, 8]. However, such error indicators lack theoretical justification as soon as the problem is not single-component and diffusion dominated. In bunsen flame simulations, error propagation due to convective transport and complex chemistry couplings is extremely important and must therefore be accounted for. Another drawback of local gradient and curvature indicators is that they do not provide a quantitative assessment of the actual numerical error. Such estimates are crucial in driving approximate solutions towards convergence. Moreover, they may also provide general guidelines to calibrate experimental measurements which are also subject to uncertainties, especially if minor species are measured.

An interesting approach towards adaptive mesh generation with quantitative error control has been developed recently in the framework of finite element methods and optimal

control techniques [9]. The dual weighted residual (DWR) method provides an estimate for a user specified functional of the error in terms of residuals, defined as the finite element solution re-injected into the governing equations, weighted by coefficients depending on the solution of a linearised dual problem. The dual weights account for convective error propagation and also contain the information relative to complex chemistry couplings at the flame front. The DWR method is particularly attractive because it yields a quantitative error estimate that may be split into elementwise contributions and subsequently used to generate an adaptively refined mesh. Applications to combustion problems include premixed flames in hot wall tubes and periodic slot burners with detailed chemistry [10, 11] as well as axisymmetric jet flames with simple chemistry [12].

The goal of the present paper is to derive a finite element method with adaptive mesh generation based on the DWR method to simulate laminar bunsen flames. From a computational viewpoint, one novelty of the present work is that the governing equations are discretised on unstructured triangulations, as opposed to previous work where hierarchical rectangular meshes were considered [11, 12]. From a physical viewpoint, this work is the first application of the DWR method to bunsen flames with detailed chemistry and transport. Our physical model indeed incorporates both complex chemical kinetics and detailed multicomponent transport algorithms, including non-diagonal molecular diffusion and thermal diffusion. In order to evaluate the usefulness of the proposed methodology for bunsen flame simulation, two series of results are investigated for rich and lean H_2/Air bunsen flames. We first assess numerical errors on a series of adaptively refined meshes corresponding to various error output functional. We then investigate the impact of injection velocities on bunsen flame shape.

The paper is organised as follows. The equations governing laminar bunsen flames are presented in Section 2. Numerical methods are described in Section 3. Section 4 contains our numerical results. Conclusions are drawn in Section 5.

2. Physical modelling

This section specifies our physical model for laminar bunsen flames, including conservation equations, complex chemistry with finite rate kinetics, multicomponent transport algorithms and boundary conditions.

2.1. Conservation equations

The equations governing laminar bunsen flames express the conservation of species mass, momentum and energy. These equations are considered here in their axisymmetric and steady form. Furthermore, since the flow velocities are significantly smaller than the sound speed, we shall use the isobaric (or low Mach) flame approximation and split the pressure into a spatially varying hydrodynamic pressure p plus a constant thermodynamic pressure p_0 in such a way that the ratio p/p_0 scales as the square of the Mach number [13, 14]. Letting ns be the number of species in the mixture, one may choose for the dependent

unknowns the $(ns+4)$-vector u with components

$$u = (p, v_r, v_z, T, y_1, \ldots, y_{ns})\,, \tag{1}$$

where v_r and v_z denote respectively the radial and axial velocity components, T the temperature and $y_1, \ldots, y_{ns}$ the species mass fractions.

The governing equations may be written in the general form

$$\mathcal{L}_i(u) := \mathcal{F}_i^0(u) + \frac{1}{r}\partial_r(r\mathcal{F}_i^r(u)) + \partial_z(\mathcal{F}_i^z(u)) = 0\,, \qquad 1 \le i \le ns+4\,, \tag{2}$$

where ∂_r and ∂_z denote differentiation with respect to the radial coordinate r and the axial coordinate z respectively. The zero-order fluxes $\mathcal{F}^0(u)$ are given by

$$\mathcal{F}^0(u) = \begin{pmatrix} \partial_r v_r + \partial_z v_z + \frac{v_r}{r} + \frac{1}{\rho}\left(v_r\partial_r\rho + v_z\partial_z\rho\right) \\ \rho(v\cdot\partial)v_r - \frac{p}{r} - \frac{2}{3}\frac{\eta}{r}(\partial_r v_r + \partial_z v_z + \frac{v_r}{r}) + 2\frac{\eta}{r^2}v_r \\ \rho(v\cdot\partial)v_z + \rho g \\ \rho c_p(v\cdot\partial)T - \omega_T \\ \rho(v\cdot\partial)y_i - \omega_i \end{pmatrix}, \tag{3}$$

where ρ denotes the density given by the ideal gas law

$$\rho = \frac{p_0 m}{RT}\,. \tag{4}$$

In the above equations, m is the mean molecular mass of the mixture, R the universal gas constant, $v\cdot\partial = v_r\partial_r + v_z\partial_z$ the convective derivative, $g > 0$ the gravity constant, c_p the specific, constant pressure heat capacity of the mixture, ω_T the enthalpy production rate and ω_i the mass production rate of the ith species. The first-order radial and axial fluxes $\mathcal{F}^r(u)$ and $\mathcal{F}^z(u)$ may be expressed as

$$\mathcal{F}^r(u) = \begin{pmatrix} 0 \\ -2\eta\partial_r v_r + p + \frac{2}{3}\eta(\partial_r v_r + \partial_z v_z + \frac{v_r}{r}) \\ -\eta(\partial_r v_z + \partial_z v_r) \\ q_r \\ f_{i,r} \end{pmatrix}, \tag{5}$$

and

$$\mathcal{F}^z(u) = \begin{pmatrix} 0 \\ -\eta(\partial_r v_z + \partial_z v_r) \\ -2\eta\partial_z v_z + p + \frac{2}{3}\eta(\partial_r v_r + \partial_z v_z + \frac{v_r}{r}) \\ q_z \\ f_{i,z} \end{pmatrix}, \tag{6}$$

where η is the shear viscosity, $q = (q_r, q_z)$ the thermal part of the heat flux vector and $f_i = (f_{i,r}, f_{i,z})$ the mass diffusion flux of the ith species. The enthalpy production rate is given by

$$\omega_T = -\sum_{i=1}^{ns} h_i\omega_i - \sum_{i=1}^{ns} c_{p,i}(f_{i,r}\partial_r T + f_{i,z}\partial_z T)\,, \tag{7}$$

where h_i is the specific enthalpy of the ith species and $c_{p,i}$ its specific, constant pressure heat capacity. Because of overall mass conservation, the governing equation for the last chemical species (typically a dilutant such as N_2) is actually written as $\mathcal{L}_{ns+4}(u) := \sum_{j=1}^{ns} y_j - 1$.

2.2. Thermochemistry

Thermochemistry properties are computed using vectorised and highly optimised versions of the Chemkin package [15]. The species specific enthalpies and constant pressure heat capacities are evaluated as a function of the temperature using polynomial fits with tabulated coefficients. The species production rates result from a complex reaction mechanism and may be expressed as

$$\omega_i = m_i \sum_{r=1}^{nr} \left(\nu_{ir}^b - \nu_{ir}^f\right) \left(K_{f,r} \prod_{j=1}^{ns} c_j^{\nu_{jr}^f} - K_{b,r} \prod_{j=1}^{ns} c_j^{\nu_{jr}^b} \right) , \tag{8}$$

where m_i is the molecular mass of the ith species, nr the number of elementary reactions, ν_{ir}^f and ν_{ir}^b are respectively the forward and backward stoichiometric coefficient for the ith species in the rth elementary reaction, $K_{f,r}$ and $K_{b,r}$ respectively the forward and backward reaction constant for the rth elementary reaction and c_j the concentration of the jth chemical species. The forward reaction constant $K_{f,r}$ is evaluated as a function of the temperature using a modified Arrhenius expression. The backward constant is recovered from the relation $K_{b,r} = K_{f,r}/K_{e,r}$ where $K_{e,r}$ is the equilibrium constant given by the thermodynamics. In our simulations, we consider a reaction mechanism involving $ns = 9$ species H_2, O_2, H_2O, H, O, OH, HO_2, H_2O_2 and N_2 participating in $nr = 19$ elementary reactions [16].

2.3. Multicomponent transport algorithms

From the kinetic theory of dilute polyatomic gas mixtures and the first-order Enskog-Chapman expansion, the fluxes expressing multicomponent transport of species mass, momentum and energy take on the form [17]

$$\left\{ \begin{array}{rcl} f_i &=& -\displaystyle\sum_{j=1}^{ns} \rho y_i D_{ij} (\partial x_j + x_j \widetilde{\chi}_j \partial \log T) \,, \quad 1 \le i \le ns \,, \\ S &=& -2\eta\varepsilon + \frac{2}{3}\eta \mathrm{tr}(\varepsilon) I \,, \\ q &=& -\lambda \partial T + RT \displaystyle\sum_{j=1}^{ns} \frac{\widetilde{\chi}_j}{m_j} f_j \,, \end{array} \right. \tag{9}$$

where x_j is the mole fraction of the jth species, $\partial = (\partial_r, \partial_z)$ the gradient operator, $D = (D_{ij})_{1 \le i,j \le ns}$ the multicomponent diffusion matrix, $\widetilde{\chi} = (\widetilde{\chi}_j)_{1 \le j \le ns}$ the rescaled thermal diffusion ratios, ε the strain tensor given by

$$\varepsilon = \begin{pmatrix} \partial_r v_r & 0 & \frac{1}{2}(\partial_r v_z + \partial_z v_r) \\ 0 & \frac{v_r}{r} & 0 \\ \frac{1}{2}(\partial_r v_z + \partial_z v_r) & 0 & \partial_z v_z \end{pmatrix} , \tag{10}$$

and λ the thermal conductivity. For the sake of simplicity, the viscous tensor S has already been eliminated from the physical fluxes (3)–(5). The multicomponent diffusion matrix D is symmetric positive semidefinite with kernel spanned by the vector $(y_1, \ldots, y_{ns})$ and the rescaled thermal diffusion ratios are such that $\sum_{j=1}^{ns} x_j \widetilde{\chi}_j = 0$. As a result, the species diffusion fluxes are compatible with the overall mass conservation constraint

$$\sum_{j=1}^{ns} f_j = 0\,. \tag{11}$$

Non-diagonal molecular diffusion and thermal diffusion are accounted for in the multicomponent fluxes (9) because these effects often have a sizeable impact on laminar and turbulent H_2/Air flame structures [18, 19, 20].

The multicomponent transport coefficients D, $\widetilde{\chi}$, λ and η depend on the temperature and the species mass fractions. In the framework of the kinetic theory of gases, these coefficients may be expressed in terms of the solution of constrained singular linear systems. The mathematical structure of these systems has been investigated in [17, 21]. In particular, the transport coefficients can be expanded as convergent series whence cost-effective, accurate approximate expressions are derived by truncation [22]. Optimised transport algorithms for flame codes are implemented in [23]. We may evaluate the shear viscosity by performing one conjugate gradient iteration on the usual transport linear system of size ns preconditioned by its diagonal. The resulting expression is more accurate and less computationally expensive than the empirical Wilke approximation. The thermal conductivity and the rescaled thermal diffusion ratios may be evaluated from a linear system of size ns. This system, based upon a reduced expansion basis for the species perturbed distribution functions, is half the size of the classical linear system usually considered in the literature. Three conjugate gradient iterations with diagonal preconditioning are performed to evaluate λ and $\widetilde{\chi}$. Finally, the species mass diffusion fluxes are evaluated from the Stefan-Maxwell-Boltzmann equations. The associated system matrix is symmetric positive semidefinite and of size ns. A symmetric positive definite matrix may be easily constructed upon adding a symmetric rank-one perturbation. Let Δ be the matrix with coefficients $\Delta_{ij} = -x_i x_j / \mathcal{D}_{ij}$, for $1 \leq i, j \leq ns$ and $i \neq j$, and $\Delta_{ii} = -\sum_{j \neq i} \Delta_{ij}$ where $\mathcal{D}_{ij}$ is the binary diffusion coefficient for species pair (i, j). Let $Y = (y_1, \ldots, y_{ns})$ be the mass fraction vector and let $d = (d_1, \ldots, d_{ns})$ be the vector with components $d_i = \partial x_i + x_i \widetilde{\chi}_i \partial \log T$. The positive definite version of the Stefan-Maxwell-Boltzmann equations we consider may be written as: seek $\zeta \in \mathbb{R}^{ns}$ such that

$$(\Delta + Y \otimes Y)\zeta = -d\,, \tag{12}$$

and the species mass diffusion fluxes are then given by $f_i = \rho y_i \zeta_i$. They satisfy the constraint (11) by construction.

2.4. Boundary conditions

The governing equations discussed in the previous sections are posed on a computational domain Ω which in our simulations will be a rectangular domain $[0, L_r] \times [0, L_z]$. The boundary $\partial\Omega$ is split into its 4 sides numbered clockwise, with $\partial\Omega_1$ denoting the axis of

symmetry ($r = 0$), $\partial\Omega_2$ the outflow boundary ($z = L_z$), $\partial\Omega_3$ the far field ($r = L_r$) and $\partial\Omega_4$ the inflow boundary ($z = 0$). The physical configuration is depicted in figure 1.

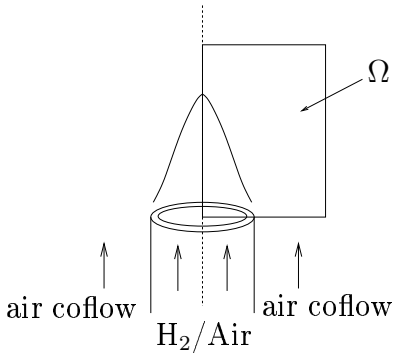

Figure 1. Physical configuration for the axisymmetric bunsen flame problem (not in scale)

The governing equations are closed by the following boundary conditions:

- axis of symmetry

$$\partial_r p = 0\,, \quad v_r = 0\,, \quad \partial_r v_z = 0\,, \quad \partial_r T = 0\,, \quad \partial_r y_i = 0\,, \tag{13}$$

- outflow

$$p = 0\,, \quad v_r = 0\,, \quad \partial_z v_z = 0\,, \quad \partial_z T = 0\,, \quad \partial_z y_i = 0\,, \tag{14}$$

- far field

$$\partial_r p = 0\,, \quad v_r = 0\,, \quad \partial_r v_z = 0\,, \quad \partial_r T = 0\,, \quad \partial_r y_i = 0\,, \tag{15}$$

- inflow

$$\begin{cases} v_r = 0\,, \quad v_z = v^d(r)\,, \quad T = T^d\,, \\ \rho^d(r)\, v^d(r)(y_i - y_i^d(r)) + f_{i,z} = 0\,, \end{cases} \tag{16}$$

where the superscript ^{d} indicates prescribed values.

The premixed fresh gas mixture is injected through a tube with inner radius $r_i = 2$ mm and outer radius $r_o = 2.5$ mm. Both the burner flow and the air coflow are of plug type with exponential boundary layer

$$v^d(r) = \begin{cases} v_b(1 - \exp((r - r_i)/\delta) & r \le r_i\,, \\ 0 & r_i \le r \le r_o\,, \\ v_c(1 - \exp((r_o - r)/\delta) & r_o \le r\,, \end{cases} \tag{17}$$

and gradient parameter $\delta = 0.5$ mm. The burner lips, the fresh mixture flow and the air coflow are kept at a temperature of $T^d = 300$ K.

3. Numerical methods

This section describes the numerical methods considered in this paper: the finite element discretisation of the governing equations, the a posteriori error estimate based on the dual weighted residual method and the algorithmic aspects related to adaptive grid generation.

3.1. Finite element discretisation

Let $\mathcal{T}$ be a triangulation (with no hanging nodes) of the computational domain Ω. Let P_c^1 be the conforming finite element space with linear trial functions given by

$$P_c^1 = \Big\{ \phi \in C^0(\overline{\Omega}),\ \forall K \in \mathcal{T},\ \phi_{|K} \in \mathbb{P}^1 \Big\}, \tag{18}$$

where $\mathbb{P}^1$ is the set of polynomials of degree ≤ 1. Set also $P_{c,0}^1 = \{ \phi \in P_c^1,\ \phi_{|\partial\Omega} = 0 \}$ and for $1 \leq l \leq 4$, $P_{c,l}^1 = \{ \phi \in P_c^1,\ \phi_{|\partial\Omega_l} = 0 \}$.

We seek for a discrete solution $u_* = (p_*, v_{r*}, v_{z*}, T_*, y_{1*}, \ldots, , y_{ns*}) \in u_*^d + \mathbb{V}$ where u_*^d accounts for non-homogeneous Dirichlet boundary conditions, that is velocity and temperature at inflow, and

$$\mathbb{V} = P_{c,2}^1 \times P_{c,0}^1 \times P_{c,4}^1 \times P_{c,4}^1 \times \big(P_c^1\big)^{ns}\ . \tag{19}$$

In the Galerkin formulation, the approximate solution u_* is required to satisfy the discrete equations

$$\forall \phi = (\phi_1, \ldots, \phi_{ns+4}) \in \mathbb{V}\,, \qquad a(u_*; \phi) = 0\,, \tag{20}$$

where

$$\begin{aligned} a(u_*;\phi) &= \textstyle\sum_{i=1}^{ns+4} \int_\Omega \mathcal{F}_i^0(u_*) \cdot \phi_i \, r dr dz \\ &- \textstyle\sum_{i=1}^{ns+4} \int_\Omega \mathcal{F}_i^r(u_*) \cdot \partial_r \phi_i \, r dr dz - \int_\Omega \mathcal{F}_i^z(u_*) \cdot \partial_z \phi_i \, r dr dz \\ &+ \textstyle\sum_{i=1}^{ns} \int_{\partial\Omega_4} \rho^d v^d (y_i - y_i^d) \phi_{4+i} \, r dl\,. \end{aligned} \tag{21}$$

The form a is nonlinear in u_* but linear in ϕ.

Some additional terms must be added to the form a in order to stabilise the Galerkin finite element formulation (20). The stabilisation is designed to match the following targets:

- least-squares control of streamline derivatives for velocity components, temperature and species mass fractions [24, 25, 26];
- least-squares control of hydrodynamic pressure gradient and of continuity equation [27, 28];
- high-order shock capturing term to control spurious oscillations near sharp fronts [29].

In order to write the stabilisation terms, it is convenient to introduce the following numerical parameters

$$\left\{ \begin{array}{l} \beta = (\beta_r, \beta_z) = (\rho_* v_{r*}, \rho_* v_{z*})\,, \quad \beta^\perp = (\beta_z, -\beta_r)\,, \quad |\beta| = (\beta_r^2 + \beta_z^2)^{1/2}, \\ \delta_{sd} = \dfrac{1}{2}\Big(\dfrac{\delta}{h^2} + \dfrac{|\beta|}{h}\Big)^{-1}, \quad \delta = 10^{-5}, \\ \delta_{cd} = 0.4 h^{1/2} \delta_{sd}\,, \\ \delta_{div} = 4h|\beta|\,, \end{array} \right. \tag{22}$$

where ρ_* is the density evaluated from the approximate solution u_*. All the numerical parameters in (22) are computed locally in each triangle $K \in \mathcal{T}$ at the centre of gravity. Because the Prandtl number and the species Lewis numbers are not significantly different from unity, the same reference diffusion coefficient δ is used for momentum, energy and

species mass. This approximation improves significantly the conditioning of the Jacobian matrices that are considered when solving the discrete equations while keeping the correct asymptotic behaviour for the streamline diffusion coefficient δ_{sd}.

The stabilisation form may be expressed locally over a triangle $K \in \mathcal{T}$ as

$$\begin{aligned} b_K(u_*;\phi) &= \int_K \textstyle\sum_{i=4}^{ns+3} \delta_{sd}\mathcal{L}_i(u_*)(\beta\cdot\partial\phi_i)\, r dr dz \\ &+ \int_K \delta_{sd}\Big(\mathcal{L}_2(u_*)(\beta\cdot\partial\phi_2+\partial_r\phi_1)+\mathcal{L}_3(u_*)(\beta\cdot\partial\phi_3+\partial_z\phi_1)\Big)\, r dr dz \\ &+ \int_K \delta_{div}\mathcal{L}_1(u_*)\Big(\partial_r\phi_2+\tfrac{\phi_2}{r}+\partial_z\phi_3+\tfrac{v_{r*}}{T_*}\partial_r\phi_4+\tfrac{v_{z*}}{T_*}\partial_z\phi_4\Big)\, r dr dz \\ &+ \int_K \delta_{cd}\Big((\beta^\perp\cdot\partial v_{r*})(\beta^\perp\cdot\partial\phi_2)+(\beta^\perp\cdot\partial v_{z*})(\beta^\perp\cdot\partial\phi_3)\Big)\, r dr dz \\ &+ \int_K \delta_{cd}\Big((\beta^\perp\cdot\partial T_*)(\beta^\perp\cdot\partial\phi_4)+\textstyle\sum_{i=1}^{ns-1}(\beta^\perp\cdot\partial y_{i*})(\beta^\perp\cdot\partial\phi_{4+i})\Big)\, r dr dz\,. \end{aligned} \tag{23}$$

The first two lines in the r.h.s. of (23), which correspond to the streamline diffusion method and the least-squares control of the hydrodynamic pressure gradient, have been considered in a wide range of applications involving convection-dominated flows or pressure-velocity instabilities due to the same order of discretisation for both variables. The third line yields a least-squares control of the low-Mach continuity equation and is introduced in this work as an extension of the stabilisation terms usually considered for incompressible flows. The last two lines are high-order, shock capturing terms whose function is to help preserve mass fraction positivity in the vicinity of sharp fronts. Note that only crosswind diffusion terms are considered.

Since the residuals of the governing equations $\mathcal{L}_i(u_*)$ are evaluated elementwise and the approximate solution u_* is linear in each triangle, second derivatives due to diffusion fluxes vanish identically. A further simplification is introduced by neglecting the spatial derivatives of multicomponent transport coefficients in the local residuals. We thus consider local stabilisation terms $\widetilde{b}_K(u_*;\phi)$ obtained from (23) upon substituting the residuals $\mathcal{L}_i(u_*)$ by the local residuals $\mathcal{R}_i(u_*)$ given by

$$\begin{cases} \mathcal{R}_1(u_*) = \partial_r v_r + \partial_z v_z + \frac{v_r}{r} + \frac{1}{\rho}\,(v_r\partial_r\rho + v_z\partial_z\rho) \\ \mathcal{R}_2(u_*) = \rho(v\cdot\partial)v_r + \partial_r p - \frac{4}{3}\frac{\eta}{r}(\partial_r v_r - \frac{v_r}{r}) \\ \mathcal{R}_3(u_*) = \rho(v\cdot\partial)v_z + \partial_z p + \rho g - \frac{\eta}{r}(\partial_r v_z + \frac{1}{3}\partial_z v_r) \\ \mathcal{R}_4(u_*) = \rho c_p(v\cdot\partial)T + \frac{q_r}{r} - \omega_T \\ \mathcal{R}_{4+i}(u_*) = \rho(v\cdot\partial)y_i + \frac{f_{i,r}}{r} - \omega_i \end{cases} \tag{24}$$

the r.h.s. being evaluated using the approximate solution u_*. The stabilised FEM formulation then consists in seeking $u_* \in u_*^0 + \mathbb{V}$ such that

$$\forall \phi \in \mathbb{V}\,, \qquad a(u_*;\phi) + \sum_{K\in\mathcal{T}} \widetilde{b}_K(u_*;\phi) = 0\,. \tag{25}$$

3.2. A posteriori error estimation

Let $e = (e_1, \ldots, e_{ns+4})$ be the error with components $e_i = u_i - u_{*i}$, $1 \leq i \leq ns+4$. Given a function $\psi \in L^2(\Omega)^{ns+4}$, our goal is to estimate the error output measure

$$\mathcal{J}(e) = \int_\Omega (\psi \cdot e)\, r dr dz\,, \tag{26}$$

in terms of computable quantities, i.e., only depending on the data, the mesh and the approximate solution. For instance, the functional $\mathcal{J}$ may be of the form

$$\mathcal{J}_{m,\omega}(e) = \frac{1}{|\omega|} \int_\omega e_m\, r dr dz\,, \tag{27}$$

where m denotes a solution component with $1 \leq m \leq ns+4$, ω a subdomain of the computational domain Ω and $|\omega|$ its measure. In this way, one controls the average error on a given solution component and over a specified region of the flow. The subdomain ω may typically cover the flame front or follow a line along which experimental measurements are made.

An a posteriori estimate of the quantity $\mathcal{J}(e)$ may be derived in the framework of the dual weighted residual method. The estimate takes on the form

$$\mathcal{J}(e) \leq \sum_{K \in \mathcal{T}_h} \eta_K\,, \tag{28}$$

where we have introduced the local error indicators

$$\eta_K = \sum_{i=1}^{ns+4} r_{K,i} w_{K,i}\,. \tag{29}$$

Here, the quantities $r_{K,i}$ are finite element residuals given by

$$r_{K,i} = h_K \|\mathcal{L}_i(u_*)\|_K + \frac{1}{2} h_K^{1/2} \|[(\mathcal{F}_i^r, \mathcal{F}_i^z) \cdot n]\|_{\partial K}\,, \tag{30}$$

where h_K is the diameter of K, ∂K its boundary, n its outward normal and $[(\mathcal{F}_i^r, \mathcal{F}_i^z) \cdot n]$ the jump of the normal diffusion fluxes across ∂K in the direction of n. The quantities $w_{K,i}$ are weights evaluated from the solution of the linearised dual problem: seek $\xi_* \in \mathbb{V}$ such that

$$\forall \phi \in \mathbb{V}\,, \qquad a'(u_*; \phi, \xi_*) + \sum_{K \in \mathcal{T}} \widetilde{b}'_K(u_*; \phi, \xi_*) = \mathcal{J}(\phi)\,, \tag{31}$$

where $a'(u_*; \phi, \cdot)$ is the Gateaux derivative of a in the direction of ϕ evaluated at u_* and a similar notation is used for $\widetilde{b}'_K$.

In practice, the finite element residuals $r_{K,i}$ are approximated as follows

$$r_{K,i} \simeq h_K^2 r_{|G(K)}^{1/2} |\mathcal{R}_i(u_*)|_{G(K)} + \frac{1}{2} \sum_{e \in \partial K} h_K r_{|G(K)}^{1/2} |[(\mathcal{F}_i^r, \mathcal{F}_i^z) \cdot n]|_e\,, \tag{32}$$

where $G(K)$ is the centre of gravity of K. Furthermore, the weights $w_{K,i}$ are approximated as

$$w_{K,i} \simeq h_K^2 r_{G(K)}^{1/2} D_K^2 \xi_{*i}\,, \tag{33}$$

where $D^2_K\xi_{*i}$ is a local upper bound to the second derivatives of ξ_{*i}. On unstructured meshes, this approximation is computed using a patch of elements around each triangle K. Let $\mathcal{T}_j$ be the set of triangles in $\mathcal{T}$ containing vertex j. Let s_* be the smoothing operator

$$s_* : \phi \in P^0 \mapsto s_*\phi = \sum_{j=1}^{nno} \phi_j N_j \in P^1_c \,, \tag{34}$$

where P^0 is the space of piecewise constant functions and

$$\phi_j = \frac{\sum_{K\in\mathcal{T}_j} |K|\phi_{|T}}{\sum_{K\in\mathcal{T}_j} |K|} \,, \tag{35}$$

where $|K|$ is the measure of K. Second derivatives are then approximated by differentiating the local P^1 reconstruction of the first-order derivatives of ξ_{*i}, yielding the expression

$$D^2_K\xi_{*i} = \max\Big(|\delta^{rr}_K\xi_{*i}|, |\delta^{zz}_K\xi_{*i}|, \frac{1}{2}|\delta^{rz}_K\xi_{*i} + \delta^{zr}_K\xi_{*i}|, \frac{1}{r_{|G(K)}}|\partial_r\xi_{*i|K}|\Big) \,, \tag{36}$$

where $\delta^{\alpha\beta}_K\xi_{*i} = \partial_\alpha(s_*\partial_\beta\xi_{*i})_{|K}$ for $\alpha, \beta \in \{\, r, z \,\}$.

3.3. Adaptive mesh refinement

The meshes considered in this work are fully unstructured, quasi-Delaunay triangulations generated from the procedure described in [30]. The mesh generator uses two input files: the first one specifies the trace of the mesh on the boundary $\partial\Omega$ and is referred to as the boundary mesh file. The second one specifies the desired mesh size around a set of points inside Ω and is referred to as the background mesh file.

The core of the adaptive mesh refinement procedure is to create boundary and background mesh files from the information provided by the local error indicators η_K. The adaptive algorithm involves three steps:

(i) compute desired mesh sizes

$$h'_K = f(\eta_K)h_K \,, \tag{37}$$

where for instance, $f(\eta_K) = \frac{1}{2}$ if $\eta_K \leq TOL$ and $f(\eta_K) = 1$ otherwise. The function f may also take values larger than 1 for very small η_K in order to allow for local mesh coarsening. An error balancing method is employed in which the tolerance TOL is evaluated as follows

$$TOL = \frac{1}{2}\frac{1}{nt}\sum_{K\in\mathcal{T}} \eta_K \,,$$

where nt is the number of triangles in the current mesh;

(ii) the boundary mesh file is determined directly from the quantities h'_K using the triangles having at least an edge located on $\partial\Omega$;

(iii) the background mesh file is also directly generated from the provisional h'_K's. In order to avoid excessive specifications in this file, a layering algorithm is employed in which the desired mesh size of a given triangle is written to the background mesh file only if its value is sufficiently different from that of the neighbouring elements. The fluctuation test is for instance $|\log(h'_{K_1}/h'_{K_2})| \geq \log\gamma$ with parameter $\gamma = 1.5$.

3.4. Numerical solution methodology

The discrete equations (25) are conveniently recast into a system of nonlinear equations upon introducing the decomposition

$$u_{*i} = \sum_{j=1}^{nno} U_{i,j} N_j \,, \qquad 1 \le i \le ns+4 \,, \tag{38}$$

where nno is the number of mesh vertices (including boundary ones) and N_j the Lagrange nodal basis function associated with vertex j, $1 \le j \le nno$. For $1 \le i \le ns+4$ and $1 \le j \le nno$, let $\phi_{i,j} \in \mathbb{V}$ be the test function with components $(\delta_{ik} N_j)_{1 \le k \le ns+4}$ where δ_{ik} is the Kronecker symbol. The discrete unknowns form a vector $U \in \mathbb{R}^{(ns+4)*nno}$ with components $U_{i,j}$ satisfying the nonlinear discrete equations

$$F_{i,j}(U) = a(u_*; \phi_{i,j}) + \sum_{K \in \mathcal{T}} \widetilde{b}_K(u_*; \phi_{i,j}) = 0 \,. \tag{39}$$

The residuals $F_{i,j}(U)$ are evaluated using numerical quadratures with 3 Gauss points located at midpoints of triangle edges.

The residual equations (39) are written in vector form $F(U) = 0$ and an approximate solution is obtained using a damped Newton's method. Given an initial guess U^0, the damped Newton's method yields the sequence of iterates

$$\partial_U F(U^k)(\overline{U}^{k+1} - U^k) = -\sigma^k F(U^k) \,, \tag{40}$$

where $\partial_U F(U^k)$ is the Jacobian matrix of F evaluated at U^k, $\overline{U}^{k+1}$ the provisional Newton iterate at the $(k+1)$st iteration and σ^k the damping parameter. The Newton iterate U^{k+1} is then evaluated from $\overline{U}^{k+1}$ using a projection on the cone Λ of positive mass fractions. Convergence of Newton's method is achieved when the norm of the update vector $U^{k+1} - U^k$ is brought below a prescribed tolerance, typically 10^{-4}. The projection on Λ is compatible with the convergence of Newton's method only if its numerical convergence domain is sufficiently close to Λ. This is indeed the case in our computations thanks to the shock capturing terms used to stabilise the Galerkin formulation.

At each Newton step (40), the Jacobian matrix is assembled from perturbed residual evaluations and the linear system is solved approximately using a preconditioned Krylov iterative solver, typically BiCGStab with Gauss-Seidel preconditioner blocked at node level. The efficiency of the preconditioner may be enhanced by an appropriate renumbering of the mesh nodes according to the flow streamlines. Convergence is achieved when the relative linear residual has been brought below a prescribed tolerance, typically 10^{-7}. Because the source terms present in the local residuals (24) have a significant impact on the conditioning of the Jacobian matrix, it is more efficient to consider on coarse meshes a first-order streamline diffusion method in which the local species residuals only contain the convective-diffusive contribution. On fine meshes where convective-diffusive-reactive effects are adequately resolved at the flame front, the high-order expressions (24) may be used. This point will be further discussed below.

Once convergence has been achieved on a given mesh, an a posteriori estimate of the numerical error is evaluated and the local error indicators η_K given by (29) are used to

construct a new, adaptively refined, unstructured mesh. While the finite element residuals $r_{K,i}$ may be readily evaluated, the computation of the weights $w_{K,i}$ requires the solution of the following linearised dual problem: seek $X \in \mathbb{R}^{(ns+4)*nno}$ s.t.

$$\partial_U F^T \cdot X = \Psi \,, \tag{41}$$

where $\partial_U F^T$ denotes the transpose of the last Jacobian used in the damped Newton's method and where the r.h.s. $\Psi \in \mathbb{R}^{(ns+4)*nno}$ has components $\Psi_{i,j} = \mathcal{J}(\phi_{i,j})$ for $1 \leq i \leq ns+4$ and $1 \leq j \leq nno$. The nodal values of the dual solution ξ_* are then directly recovered from the components of the vector X. Note that the computational effort to solve (41) is much lower than that required to obtain the discrete solution U.

4. Numerical results

In this section we discuss our numerical results. We first investigate the numerical performance of the adaptive grid refinement methodology. Numerical errors corresponding to various output functionals are assessed on a sequence of adaptively refined, unstructured triangulations. The reference flame problem consists of a rich bunsen flame structure. We then study the influence of injection velocity profiles on rich bunsen flame shapes. Finally, we investigate a lean bunsen flame structure.

4.1. Evaluation of the adaptive methodology

We evaluate the adaptive methodology on a rich bunsen flame. The fresh H_2/Air mixture contains 75% hydrogen and 5.2% oxygen in mole fraction, corresponding to an equivalence ratio of 7.2. Injection velocities are given by $v_b = v_c = 120$ cm/s. Figure 2 presents isotherms and mole fraction isocontours for species H, OH and HO_2. The computational domain, as in all subsequent simulations, has dimensions $L_r = 1.5$ and $L_z = 25$ cm. We observe a cold dark zone circumscribed by the conically shaped premixed flame front. Although the temperature peaks at the cone tip located on the symmetry axis, its value remains nearly constant along the cone vertex, in agreement with the Clavin and Williams theory since the overall Lewis number for oxygen is about unity [31]. The flame length, defined from the point on the symmetry axis where the temperature reaches its maximum, is 1.26 cm and the flame lift-off, defined as the lowest z for which the temperature is above 1000 K is 0.11 mm. Most of the hydrogen is not consumed at the premixed flame front, but diffuses radially to create an outer diffusion flame where it burns with the oxygen supplied by the air coflow. This phenomenon is clearly visible in the H and OH mole fraction isocontours.

We investigate 4 strategies for adaptive error control based on functionals of the type (27) and illustrated in figure 3. We propose to control errors on either the temperature over subdomain $[0, 0.66] \times [0, 1.5]$, or the H mole fraction over subdomain $[0, 0.5] \times [0.19, 0.21]$, or the OH mole fraction over subdomain $[0.25, 0.35] \times [0, 1.5]$ or the HO_2 mole fraction over subdomain $[0, 0.4] \times [0, 0.2]$ (units in cm). In all cases, the adaptive procedure is started with an initial coarse unstructured triangulation containing 1599 nodes and 2954 elements (see figure 3). This mesh is constructed with very little a priori knowledge on

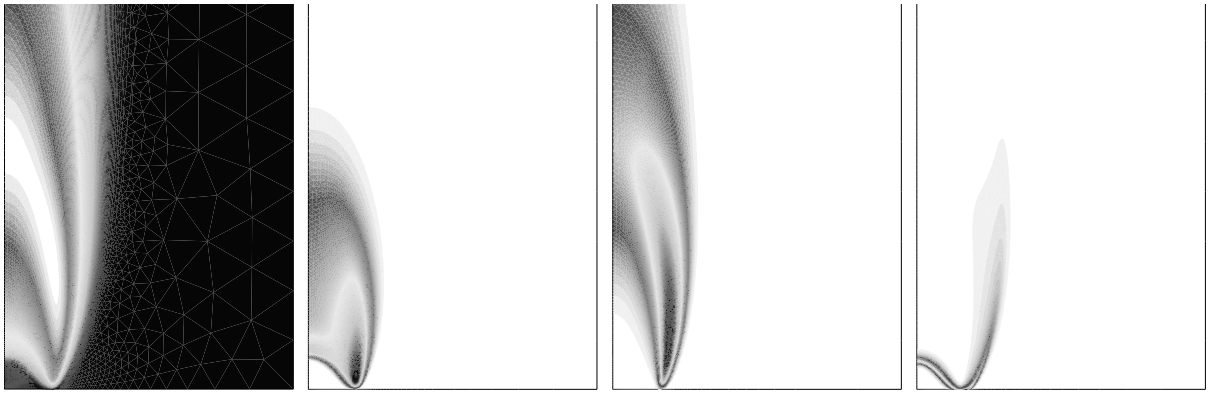

Figure 2. From left to right: isotherms and mole fraction isocontours for species H , OH and HO_2; rich bunsen flame; peak values are respectively 2038 K, 1.74e-2, 1.07e-2 and 4.39e-4; the plotting domain is $[0, 1.5] \times [0, 2]$ in cm

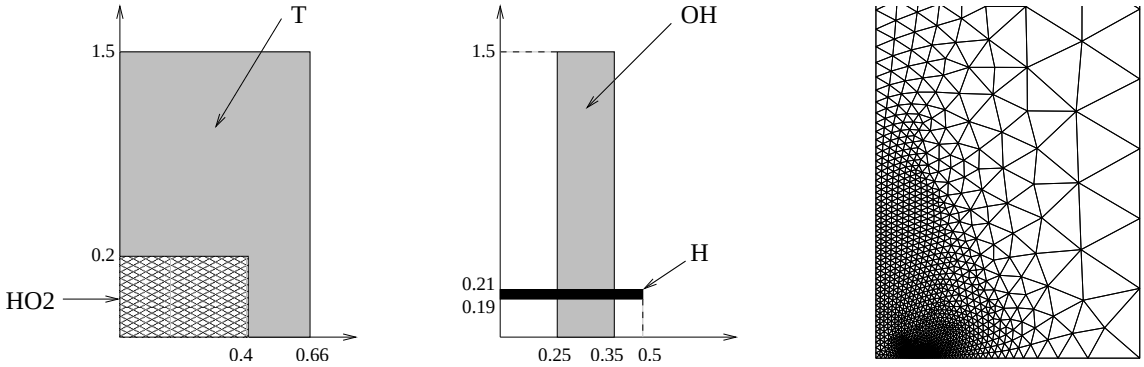

Figure 3. Illustration (not in scale) of the four numerical strategies for adaptive error control and initial coarse triangulation

the flame structure. In the boundary mesh file, we simply set h to 0.05 mm at the burner lip, to 0.3 mm at the lower left corner and to 4 mm at the upper and right boundaries. The background mesh file further imposes a desired mesh size of $h = 0.4$ mm at points $(0.2, 0.8)$ and $(0.3, 1)$ cm inside the computational domain. Four levels of refinement are then adaptively constructed by using the error functionals depicted in figure 3. Numerical results are summarised in table 1.

	T		H		OH		HO_2	
level	nodes	error	nodes	error	nodes	error	nodes	error
0	1599	1.22e-1	1599	9.35e-5	1599	1.91e-3	1599	1.30e-4
1	2826	5.55e-2	2511	4.66e-5	2800	8.82e-4	1891	3.79e-5
2	5948	2.76e-2	4687	2.33e-5	6056	4.37e-4	2771	1.25e-5
3	13987	1.40e-2	10390	1.23e-5	14844	2.34e-4	4996	4.66e-6
4	34577	7.60e-3	25387	6.73e-6	37540	1.33e-4	11638	2.14e-6

Table 1. Number of nodes of adaptively generated, unstructured meshes and a posteriori error estimates based on four different strategies for error control

Thanks to the error balancing method, the number of nodes is increased progressively from one mesh to the next finer one. The ratio in the number of nodes on subsequent triangulations generally ranges between two and three. This ratio can be compared to the one obtained by uniform refinement of structured meshes, namely 4. The error estimates decrease steadily and are brought down to levels compatible with the Newton tolerance within four adaptive refinement steps. Letting nno_l denote the number of nodes in the mesh at refinement level l, $0 \leq l \leq 4$, and err_l the corresponding estimated error, a convergence order σ may be evaluated from the expression

$$\sigma = \frac{\log(err_{l-1}/err_l)}{\log(nno_l/nno_{l-1})}\,. \tag{42}$$

For linear finite elements stabilised by the streamline diffusion method, a convergence order $\sigma = \frac{3}{4}$ is expected for the error in the L^2-norm. Provided the dual problem is solved with sufficient accuracy, the same order should be in principle observed for a posteriori estimates of functionals averaging the error over a subdomain. Convergence orders observed numerically are reported in table 2 for the various functionals. For all functionals, super-convergence is observed on the coarser meshes as a result of simultaneous improvement of primal and dual resolution as the mesh is adaptively refined. On the finer meshes, the convergence order is close to the value expected theoretically.

level	1	2	3	4
T	1.39	0.94	0.79	0.67
H	1.54	1.11	0.80	0.68
OH	1.37	0.91	0.70	0.60
HO_2	7.37	2.90	1.67	0.92

Table 2. Convergence orders observed numerically for error functionals controlling either the temperature or the H, OH or HO_2 mole fraction

Figure 4 presents the adaptive, unstructured meshes generated at level $l = 2$ for the four functionals. We observe that local mesh refinement occurs at quite different locations depending on the targeted solution component. For error control on the temperature over the whole flame, mesh refinement occurs above the burner lips, inside the premixed cone vertex and along the trailing diffusion flame. The adaptive mesh based on error control for the OH mole fraction has a comparable number of nodes because this radical is very sensitive to the temperature profile. The adaptive mesh for H error control is substantially different from the previous two triangulations and also from the shape of the H mole fraction isocontours. Indeed, because of multicomponent chemistry couplings, the accuracy achieved for the H mole fraction strongly depends on the resolution of various radical profiles inside the premixed cone vertex. This information is indeed captured by solving the dual problem, but not if local solution residuals were used solely. The adaptive mesh based on HO_2 error control concentrates most of its degrees of freedom above the burner lips and in the upstream part of the cone vertex and the trailing diffusion flame. Further downstream, the HO_2 radical is consumed and a coarser mesh may be used. To

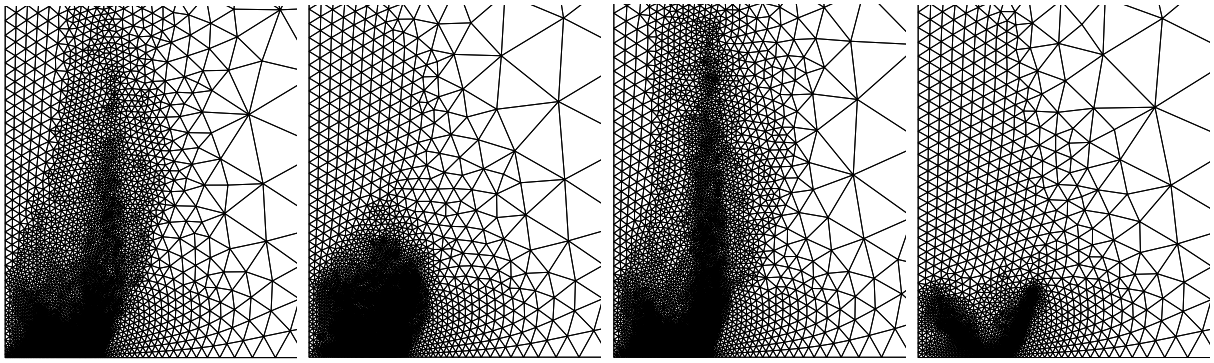

Figure 4. Unstructured meshes generated after the second adaptive refinement step; from left to right: temperature, H, OH and HO_2 error output functionals

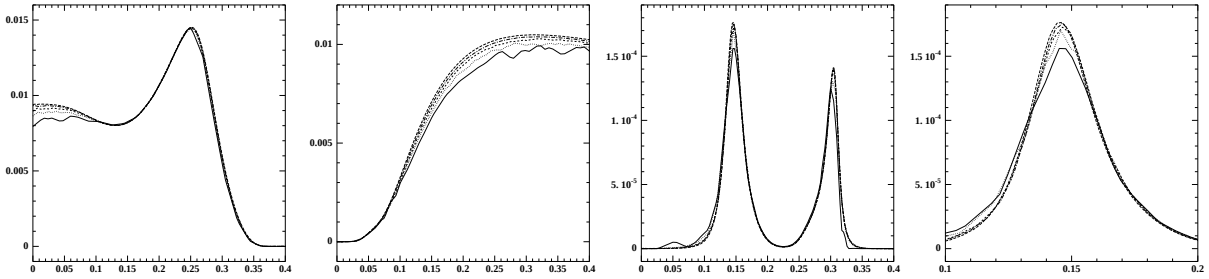

Figure 5. Solution profiles along selected lines as computed during the adaptive process; from left to right: H mole fraction at $z = 2$ mm, OH mole fraction at $r = 3$ mm, HO_2 mole fraction at $z = 0.5$ mm and a zoom of the HO_2 profile

sum up, we may recommend temperature or OH error control if the target is an accurate resolution of the overall flame structure. When the goal is to predict concentration of minor species such as H, significant computational savings may be achieved by using the appropriate error output functional. Finally, HO_2 error control appears to be an efficient strategy for computations where high resolution above the burner lips is required.

Figure 5 presents solution profiles along selected lines as computed during the adaptive process. For each radical, we compare the profiles obtained using the corresponding error functional. The improvement in capturing the radical profiles is clearly visible, especially for HO_2 where adequate resolution is achieved only at the fourth adaptive refinement step.

As discussed before, the first-order streamline diffusion method has been used in the above simulations since on coarse meshes, the inclusion of the species source terms deteriorates the conditioning of the Jacobian matrix. We have verified numerically that starting from the converged solution with first-order streamline diffusion on the finer meshes, Newton's method exhibits a smooth convergence behaviour towards the high-order solution. The a posteriori error estimates corresponding to both strategies are actually very close, confirming the adequate resolution of the inner flame structure. For instance, the error estimate on the temperature is 1.46e-2 K for the converged solution with high-order streamline diffusion on the third adaptively refined mesh. This value should be compared with the value of 1.40e-2 K obtained with the first-order method.

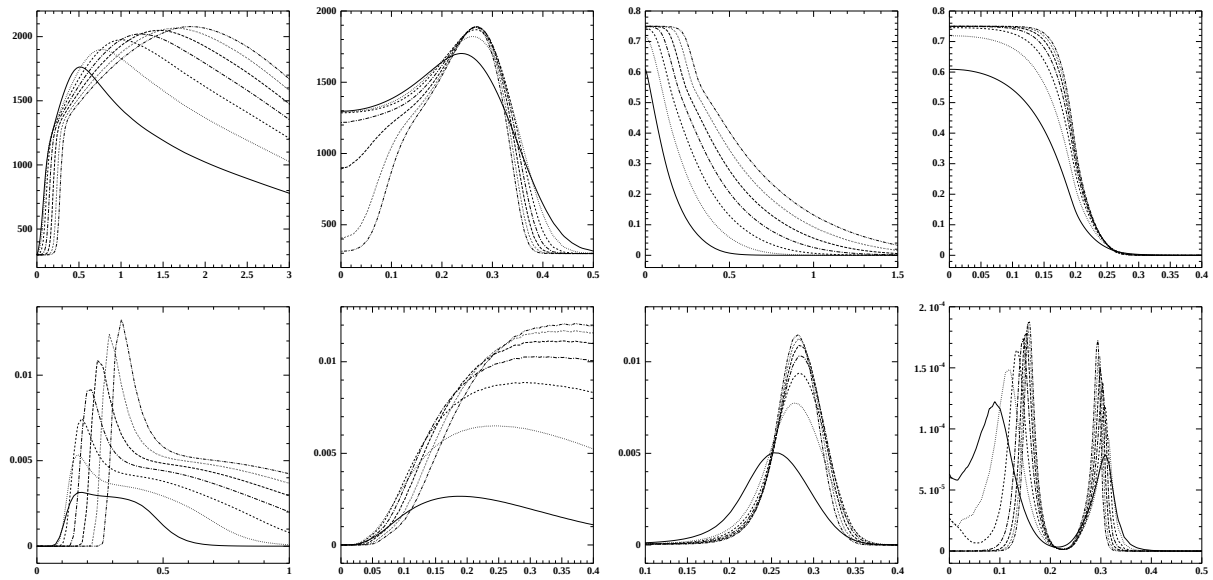

Figure 6. Profiles for various solution components along selected lines; burner and coflow velocities are varied according to (43); from left to right (top): T along symmetry line, T at $r = 2$ mm, H_2 mole fraction along symmetry line, H_2 mole fraction at $z = 0$; from left to right (bottom): H mole fraction along symmetry line, OH mole fraction at $r = 3$ mm, OH mole fraction at $z = 2$ mm and HO_2 at $z = 0.5$ mm

4.2. Impact of injection velocities on flame shapes

In this section we investigate the impact of injection velocities on rich bunsen flame structures. Numerical simulations are performed on the second, temperature based, adaptively refined mesh containing 5948 nodes and on which the error on the temperature is estimated to be 2.76e-2 K. Two experiments are considered. In the first one, both the burner and the coflow velocities are varied according to

$$v_b = v_c \in \{\, 30, 60, 90, 120, 150, 180, 210 \,\} \,\mathrm{cm/s}\,. \tag{43}$$

Figure 6 presents profiles for various solution components along selected lines. We observe important modifications in the flame length and the species profiles as the injection velocities are increased. For injection velocities lower than 90 cm/s, the premixed flame front is located very near the inflow boundary $z = 0$ and the H_2 mole fraction does not reach the value supplied by the fresh gas mixture. This phenomenon, due to upstream diffusion of intermediate species, is accounted for thanks to the inflow boundary condition (16). The peak value reached by radicals such as H, O and HO_2 is also significantly modified by the injection velocities (peak values increase with v_b and v_c). The most important changes are observed for the H profile along the symmetry line where changes by a factor of 4 are obtained.

In our second experiment, we consider the following values for the injection velocities

$$v_b = 120\,\mathrm{cm/s}\,, \quad v_c \in \{\, 30, 60, 90, 120 \,\} \,\mathrm{cm/s}\,. \tag{44}$$

Figure 7 presents profiles for various solution components along selected lines. We observe that the temperature along the symmetry axis is not significantly modified. However, as

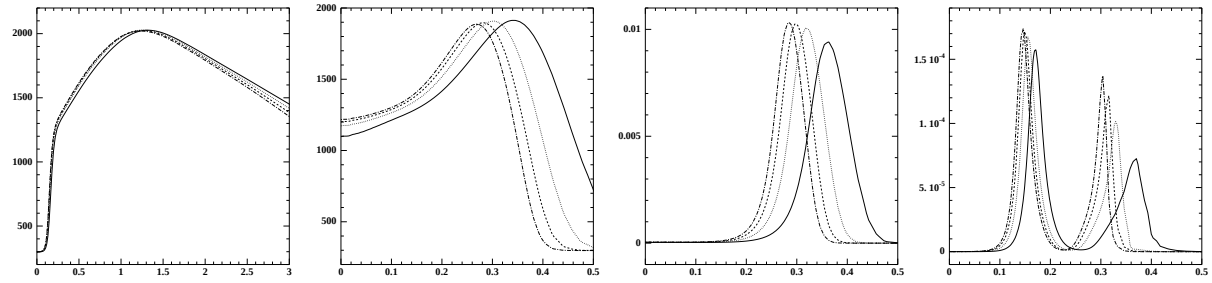

Figure 7. Profiles for various solution components along selected lines; burner and coflow velocities are varied according to (44); from left to right: T along symmetry line, T at $r = 2$ mm, OH mole fraction at $z = 2$ mm and HO_2 at $z = 0.5$ mm

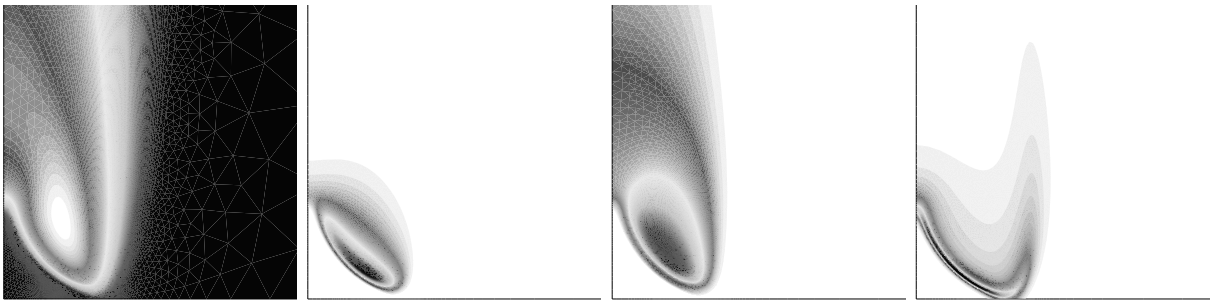

Figure 8. From left to right: isotherms and mole fraction isocontours for species H, OH and HO_2 ; lean bunsen flame; peak values are respectively 1718 K, 9.86e-3, 6.95e-2 and 4.10e-4; the plotting domain is $[0, 0.7] \times [0, 0.7]$ cm

the coflow velocity is decreased, the flame front extends more outwards radially and the radical profiles are shifted accordingly. Peak values of OH and HO_2 profiles decrease when v_c is diminished but the changes are less important than in the previous experiment. All the flame structures presented in this section have been obtained using a straightforward continuation procedure. Four to five steady Newton iterations were sufficient to achieve convergence from one flame structure to the next one.

4.3. A lean bunsen flame structure

In this section we investigate a lean bunsen flame structure. The fresh H_2/Air mixture contains 20% hydrogen and 16.8% oxygen in mole fraction, corresponding to an equivalence ratio of 0.595. Injection velocities are set to $v_b = v_c = 160$ cm/s. Figure 8 presents isotherms and mole fraction isocontours for species H, OH and HO_2. The maximum temperature is not reached on the axis, a phenomenon attributable to the overall Lewis number of hydrogen which is lower than one [31]. Mole fractions for H and OH peak slightly upstream of the premixed flame front. The HO_2 radical is present along the bunsen cone vertex, but also above the tube lip where outward diffusion of H_2 results in the formation of a small diffusion flame.

The present flame structure has been computed after four adaptive refinement steps starting with an initial mesh containing 2025 nodes. For the adaptive procedure, we

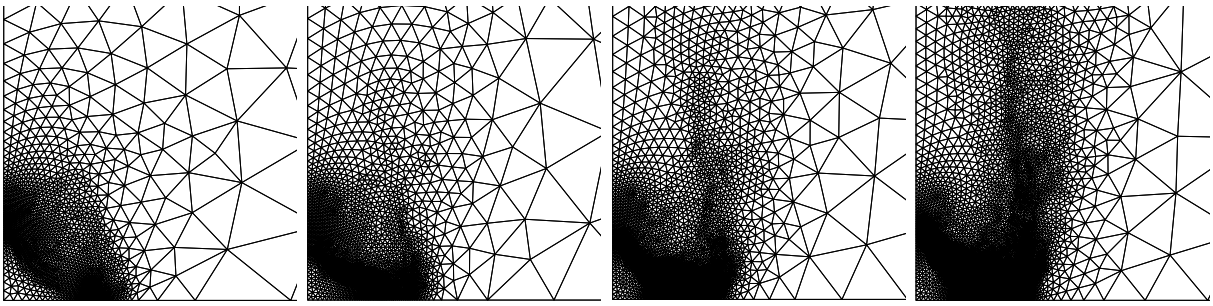

Figure 9. Adaptively refined, unstructured meshes based on temperature error control; lean bunsen flame

considered temperature error control over the same domain as for the rich flames. Figure 9, which presents the initial and the following three adaptive meshes, illustrates how the resolution of the flame front is steadily improved. A posteriori error estimates along with convergence orders are reported in table 3. As for the rich flame case, slightly super-convergence results are observed on coarser meshes.

level	0	1	2	3	4
nodes	2025	3075	6207	13966	35216
error	2.03e-2	1.17e-2	7.12e-3	3.60e-3	2.11e-3
σ	–	1.22	0.75	0.83	0.58

Table 3. Number of nodes, a posteriori error estimates and convergence orders σ observed numerically in the lean bunsen flame simulation

5. Conclusions

In this work, we have evaluated the numerical efficiency of stabilised finite element methods on adaptively refined, unstructured meshes to simulate H_2/Air bunsen flames with detailed chemistry and multicomponent transport. We have considered rich and lean flame structures with varying injection velocities. Our numerical results show that the streamline diffusion method alone can not cope efficiently with the nonlinear instabilities present in reactive fronts. Appropriate modifications include shock capturing terms ensuring positivity of the species mass fractions and first-order modifications of the method on coarse meshes. Furthermore, our numerical results show that the dual weighted residual method yields a very powerful and flexible tool to drive numerical solutions towards convergence by controlling user specified functionals of the numerical error. As such, the method is particularly attractive to be used in conjunction with experimental measurements and provides an efficient means to optimise the degrees of freedom required in simulation of bunsen flames.

References

[1] Smooke MD 1982 Solution of burner-stabilized premixed laminar flames by boundary value methods *J. Comput. Phys.* **48** 72–105.

[2] Giovangigli V and Smooke MD 1989 Adaptive continuation algorithms with application to combustion problems *Appl. Numer. Math.* **5** 305–331

[3] Coelho PJ and Pereira JCF 1993 Calculation of a confined axisymmetric laminar diffusion flame using a local grid refinement technique *Combust. Sci. Technol.* **92** 243–264

[4] de Lange HC and de Goey LPH 1994 Numerical modelling in a locally refined grid *Int. J. Num. Mech. Eng.* **37** 497–515

[5] Mallens RMM, de Lange HC, van de Ven CHJ and de Goey LPH 1995 Modeling of confined and unconfined laminar premixed flames on slit and tube burners *Combust. Sci. Technol.* **107** 387–401

[6] Somers LT and de Goey LPH 1995 A numerical study of a premixed flame on a slit burner *Combust. Sci. Technol.* **108** 121–132

[7] Bennett BAV and Smooke MD 1998 Local rectangular refinement with application to axisymmetric laminar flames *Combust. Theory Modelling* **2(3)** 221–258

[8] Day MS and Bell JB 2000 Numerical simulation of laminar reacting flows with complex chemistry *Combust. Theory Modelling* **4** 535–556

[9] Becker R and Rannacher R 2001 An optimal control approach to a posteriori error estimation in finite element methods. *Acta Numerica* Iserles A (ed.) Cambridge University Press

[10] Braack M and Rannacher R 1999 Adaptive finite element methods for low-Mach-number flows with chemical reactions *30th von Karman Institute Lecture Series on Computational Fluid Dynamics* Deconinck H (ed.)

[11] Becker R, Braack M and Rannacher R 1999 Numerical simulation of laminar flames at low Mach number by adaptive finite elements *Combust. Theory Modelling* **3** 503–534

[12] Burman E, Ern A and Giovangigli V 2001 Adaptive finite element methods for low Mach, steady, laminar combustion, *J. Comput. Phys.* submitted

[13] Williams FA 1985 *Combustion Theory* Addison-Welsey, second edition

[14] Giovangigli V 1999 *Multicomponent flow modeling* Birkhäuser, Boston

[15] Giovangigli V and Darabiha N 1988 Vector computers and complex chemistry combustion In *Proc. Conference Mathematical Modeling in Combustion and Related Topics* volume 140 pages 491–503. NATO Adv. Sci. Inst. Ser. E, Brauner C and Schmidt-Lainé C (Eds.)

[16] Miller J, Mitchell R, Smooke M, and Kee R J 1982 Toward a comprehensive chemical kinetic mechanism for the oxidation of acetylene : comparison of model predictions with results from flame and shock tube experiments *Proc. Combust. Inst.* **19** 181–196

[17] Ern A and Giovangigli V 1994 *Multicomponent Transport Algorithms* volume m 24 of *Lecture Notes in Physics*, New Series Monographs Springer-Verlag, Heidelberg

[18] Ern A and Giovangigli V 1998 Thermal diffusion effects in hydrogen-air and methane-air flames *Combust. Theory Model.* **2** 349–372

[19] Ern A and Giovangigli V 1999 Impact of detailed multicomponent transport on planar and counterflow hydrogen/air and methane/air flames *Combust. Sci. Tech.* **149** 157–181

[20] de Charentenay J and Ern A 2002 Multicomponent transport impact on turbulent premixed $H2/O_2$ flames *Combust. Theory Model.* **6** 439–462

[21] Ern A and Giovangigli V 1996 The structure of transport linear systems in dilute isotropic gas mixtures *Phys. Rev. E* **53** 485–492

[22] Ern A and Giovangigli V 1995 Fast and accurate multicomponent transport property evaluation *J. Comput. Phys.* **120** 105–116

[23] Ern A and Giovangigli V 1996 [http://www.cmap.polytechnique.fr/www.eglib], Eglib server with user's manual

[24] Brooks AN and Hughes TJR 1982 Streamline Upwind/Petrov–Galerkin formulations for convective dominated flows with particular emphasis on the incompressible Navier–Stokes equations *Comput. Methods Appl. Mech. Engrg.* **32** 199–259

[25] Johnson C, Nävert U and Pitkäranta J 1984 Finite element methods for linear hyperbolic equations *Comput. Methods Appl. Mech. Engrg.* **45** 285–312

[26] Johnson C 1987 *Numerical Solution of Partial Differential Equations by the Finite Element Method* Cambridge University Press, Cambridge

[27] Franca LP and Frey SL 1992 Stabilized finite element methods: II. The incompressible Navier–Stokes equations *Comput. Methods Appl. Mech. Engrg.* **99** 209–233

[28] Tobiska L and Verfürth R 1996 Analysis of a streamline diffusion finite element method for the Stokes and Navier–Stokes equations *SIAM J. Numer. Anal.* **33(1)** 107–127

[29] Johnson C, Schatz A and Wahlbin L 1987 Crosswind smear and pointwise error in streamline diffusion finite element methods *Math. Comp.* **49** 25–38

[30] Rebay S 1993 Efficient unstructured mesh generation by means of Delaunay triangulation and Bowyer-Watson algorithm *J. Comput. Phys.* **106** 125–138

[31] Clavin P and Williams F 1982 Effects of molecular diffusion and of thermal expansion on the structure and dynamics of premixed flames in turbulent flows of large scale and low intensity, *J. Fluid Mech.* **116** 251–282